Trans Indian Inst Met (2021) 74(10):2499–2510
https://doi.org/10.1007/s12666-021-02283-w

ORIGINAL ARTICLE

Formation and Evolution of Microstructure in Shape Memory Alloy Wire Reinforced Composites

Venkatesh Ananchaperumal[1] · **Srikanth Vedantam**[1]

Received: 3 March 2021 / Accepted: 29 April 2021 / Published online: 30 May 2021

Abstract In this work, we study the mechanical response of shape memory alloy (SMA) wire reinforced composites using a recently developed novel discrete particle model. In this model, the discrete particles interact through forces specified by the continuum thermoelastic free energy of the material. We study the formation and evolution of fine microstructure in the SMA composites with different matrix properties under thermal and mechanical loads. The effect of phase transformation and detwinning in the SMA on the overall mechanical response of the composite is studied. The elastic modulus of the matrix has a significant effect on the formation of the microstructure of the SMA. This in turn affects the overall damping response of the composite. Interestingly, in the case with high Young's modulus of the matrix, a retwinning process is observed upon unloading a detwinned wire. These results provide insights for the design and analysis of SMA composites.

Keywords Smart composites · Shape memory alloys · Thermomechanical behavior

1 Introduction

In recent years, composites are being more widely used in many applications in the aviation and automotive industries due to their relatively high stiffness-to-weight ratios compared to traditional materials [1, 2]. Some of the drawbacks of composites for structural uses have been addressed by metallic wire reinforcements [3–5]. Of the various metallic wire reinforced composites, shape memory alloy (SMA) wires are of particular interest due to their advantages [6–8].

It is widely known that two interesting kinds of behavior are observed in SMA upon mechanical and thermal loading [9–11]. At relatively high temperatures (above the transformation temperature), SMA possesses the ability to recover from large deformations upon the application of mechanical loading followed by unloading. This behavior, referred to as *pseudoelasticity*, arises due to the stress-induced transformation of the austenite phase to martensite. However, upon unloading, the austenite phase and the overall strain are completely recovered. At temperatures lower than the transformation temperature, the material undergoes an apparently plastic deformation which can be completely recovered by heating above the transformation temperature. This is due to the detwinning of the initially twinned martensite phase, which does recover during unloading. Upon heating above the transformation temperature, a phase change to austenite allows recovery of the strain. This behavior is referred to as the *shape memory effect*. The most important feature of both these effects is that, they involve the evolution of microstructural features, which play a significant role in the overall response of the material.

SMA wire reinforced composites are referred to as smart composites due their ability to change qualitative and quantitative aspects of their behavior with relatively small changes in temperature [12]. Some of the aspects of SMA composites which have been studied in detail are adaptive shape change, self-healing, damping and vibrational properties and impact resistance [13–16]. These aspects have been studied mainly through experiments and modeling [17–19]. In order to understand the microscopic aspects of

✉ Srikanth Vedantam
srikanth@iitm.ac.in

[1] Department of Engineering Design, Indian Institute of Technology Madras, Chennai 600036, India

the interactions between the SMA and matrix as well as to develop design procedures using these materials, it is essential to develop high fidelity models of SMA composites [20, 21]. It is important to understand the role of the matrix stress distributions on the microstructure of the SMA wires and conversely the effect of the microstructure on the matrix in order to design and predict the overall properties of the SMA composites.

Most of the studies heretofore have used one-dimensional phenomenological models of SMA to model the mechanical behavior of the composites [22–24]. However, in order to understand the role of the microstructure formation and evolution in the SMA, microstructural models are necessary. Microstructural models of SMA are based on phase field approaches or discrete particle models [25–27]. Recently, SMA nanocomposites have been studied using the phase field model [28, 29]. However, such models are restricted to extremely small length- and timescales. On the other hand, discrete particle models can be used for modeling bulk length- and timescales [30, 31].

In this work, we use a recently developed discrete particle model to study the formation and evolution of microstructure in SMA reinforced composites. Discrete particle approaches dispense with the continuum assumption and treat the body as a set of discrete point masses. The interactions between the point masses determine the constitutive response of the overall material. If the point masses are taken to be atoms, the interactions arise from interatomic potentials and the resulting model is referred to as molecular dynamics. While such an approach provides fundamental insights, the length- and timescales accessible to such models are too small for practical applications. On the other hand, if the point masses are taken to be larger than individual atoms, it is difficult to determine appropriate interaction potentials. In previous work, the interactions have been taken to be simple harmonic pairwise potentials. Such interactions cannot describe the complex constitutive behavior of SMAs [32, 33].

We have recently developed an alternative approach in which the interaction between the point masses is specified through the continuum free energy of the material [31, 34]. Based on the reference and current configurations of the particles, we calculate a discrete deformation tensor describing the deformation of each connected triangle of particles in the body. The total energy of the discrete system is then taken to be the continuum free energy of each of the triangles expressed as a function of the particle positions. The interaction forces then arise as a gradient of the total energy of the body. The dynamics of the particles is specified by the interaction forces derived in this manner.

Using this approach, we study SMA wire reinforced composites. The SMA wires are considered to be single crystals and perfectly bonded to the matrix. We study the nucleation and evolution of the twinned martensite upon cooling as well as the stress-induced martensitic transformation upon mechanical loading. The role of the matrix elastic modulus on the phase transformation and detwinning is also considered.

In Sect. 2, we describe the continuum interactions-based particle dynamics model (CPD) briefly following Uchimali et al. [30, 31]. A specific free energy for a phase-transforming materials is also described. In Sect. 3, we study the temperature-induced phase transformation from austenite to twinned martensite. This is followed by studies of mechanical loading of stress-induced martensitic phase transformations as well as detwinning.

2 Continuum Interaction Particle Dynamics (CPD) Model

2.1 Governing Equations

In this section, we summarize the CPD discrete particle approach following [30, 31]. The domain is discretized into a set of randomly distributed particles as shown in Fig. 1. The current positions of the particles are denoted by $\boldsymbol{y}_i(t)$. The governing equations for the particles are given by

$$m_i \frac{\mathrm{d}^2 \boldsymbol{y}_i}{\mathrm{d}t^2} + c \frac{\mathrm{d}\boldsymbol{y}_i}{\mathrm{d}t} = \boldsymbol{f}_i, \quad i = 1, 2, \ldots, N, \tag{1}$$

where m_i is the mass of the particle i, and c is a damping coefficient. The net force on the particle $i, \boldsymbol{f}_i$ arises from the interactions due to the neighboring particles. The neighboring particles are identified through Delaunay triangulation of the particles in their reference, stress-free

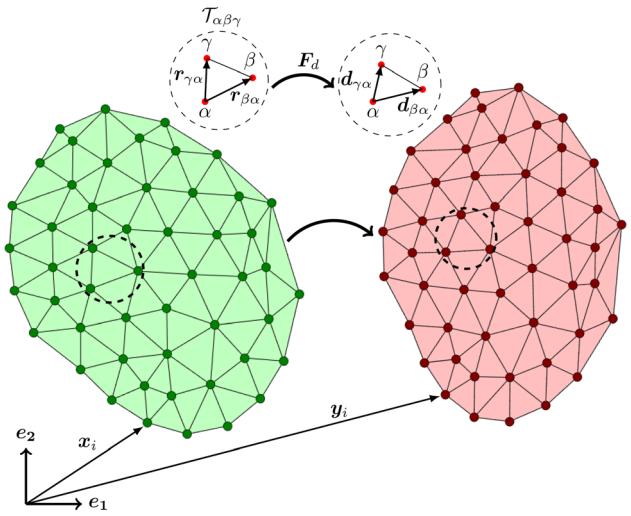

Fig. 1 Discretized body in the reference and deformed configurations. The inset shows the deformation of one triangle circled by a dashed line

configuration. The particle positions in the reference configuration are denoted by $\boldsymbol{x}_i$. We note that the particle neighbors do not change in the course of the deformation.

In order to derive the interaction forces $\boldsymbol{f}_i$ we begin by calculating a *discrete deformation tensor* $\boldsymbol{F}_d$ for each of the Delaunay triangles $\mathcal{T}_{\alpha\beta\gamma}$ comprising the particles α, β and γ. Consider the reference and deformed configurations as shown in the inset in Fig. 1. The deformation of the triangle $\mathcal{T}_{\alpha\beta\gamma}$ is characterized by the relative position vectors $\boldsymbol{r}_{\gamma\alpha} = \boldsymbol{x}_\gamma - \boldsymbol{x}_\alpha, \boldsymbol{r}_{\beta\alpha} = \boldsymbol{x}_\beta - \boldsymbol{x}_\alpha$ and $\boldsymbol{d}_{\gamma\alpha} = \boldsymbol{y}_\gamma - \boldsymbol{y}_\alpha, \boldsymbol{d}_{\beta\alpha} = \boldsymbol{y}_\beta - \boldsymbol{y}_\alpha$ in reference and current configurations, respectively. The discrete deformation tensor $\boldsymbol{F_d}$ for each Delaunay triangle $\mathcal{T}_{\alpha\beta\gamma}$ is then defined by

$$\begin{aligned} \boldsymbol{d}_{\beta\alpha} &= \boldsymbol{F}_d \boldsymbol{r}_{\beta\alpha} \\ \boldsymbol{d}_{\gamma\alpha} &= \boldsymbol{F}_d \boldsymbol{r}_{\gamma\alpha} \end{aligned} \tag{2}$$

Solving Eqs. (2) for $\boldsymbol{F}_d$ in an rectilinear coordinate frame with basis $\{\boldsymbol{e}_1, \boldsymbol{e}_2\}$, we obtain

$$\boldsymbol{F}_d = \left(\boldsymbol{d}_{\beta\alpha} \otimes \boldsymbol{e}_1 + \boldsymbol{d}_{\gamma\alpha} \otimes \boldsymbol{e}_2\right)\left(\boldsymbol{r}_{\beta\alpha} \otimes \boldsymbol{e}_1 + \boldsymbol{r}_{\gamma\alpha} \otimes \boldsymbol{e}_2\right)^{-1}, \tag{3}$$

where $\boldsymbol{a} \otimes \boldsymbol{b}$ represents the dyadic product between the two vectors $\boldsymbol{a}$ and $\boldsymbol{b}$.

The next step of the development of the interactions forces is to identify the discrete deformation tensor $\boldsymbol{F}_d$ with the continuum deformation gradient tensor $\boldsymbol{F}$. Using this identification, we can then obtain an interaction energy of the discrete model based on the *continuum constitutive behavior prescribed by a free energy density which is taken to be a function of temperature* θ *and the deformation gradient* $\boldsymbol{F}$. Specifically the continuum free energy,

$$\psi = \tilde{\psi}(\boldsymbol{E}, \theta), \tag{4}$$

where $\boldsymbol{E} = \frac{1}{2}\left(\boldsymbol{F}^T\boldsymbol{F} - \boldsymbol{1}\right)$ is the Lagrangian or Green strain tensor is expressed as a function of discrete analogue of Lagrangian strain tensor $\boldsymbol{E}_d = \frac{1}{2}\left(\boldsymbol{F}_d^T\boldsymbol{F}_d - \boldsymbol{1}\right)$ and temperature θ in the form,

$$W_{\alpha\beta\gamma} = V_{\alpha\beta\gamma}\tilde{\psi}(\boldsymbol{E}_d, \theta), \tag{5}$$

where $V_{\alpha\beta\gamma} = |\boldsymbol{r}_{\beta\alpha} \times \boldsymbol{r}_{\gamma\alpha}|$ is the volume of the triangular prism of unit depth.

The total energy of the discrete model is then $W = \sum W_{\alpha\beta\gamma}$, where the sum is taken over all Delaunay triangles in the domain. The interaction force on particle i due to all its neighbors is then given by

$$\boldsymbol{f}_i = -\partial W / \partial \boldsymbol{y}_i. \tag{6}$$

We note that the interactions specified by this process can describe very general constitutive behavior. In the following section, we present a free energy appropriate for shape memory alloys.

2.2 Free Energy for Shape Memory Alloys

Shape memory alloys are known to undergo diffusionless phase transformations between austenite and martensite phases. Following Vedantam and Abeyaratne [35], we take the austenite phase to be a square lattice and the reference configuration. The corresponding Lagrangian strain for stress free austenite is $\boldsymbol{E} = 0$. The martensite phase is obtained by stretching the reference square configuration along the two sides of the square by stretches α and β. In a two-dimensional setting, two such variants are obtained. The corresponding Lagrangian strains of the stress-free martensite variants are given by

$$\boldsymbol{E}_1 = \frac{1}{2}\begin{bmatrix} \alpha^2 - 1 & 0 \\ 0 & \beta^2 - 1 \end{bmatrix}, \quad \boldsymbol{E}_2 = \frac{1}{2}\begin{bmatrix} \beta^2 - 1 & 0 \\ 0 & \alpha^2 - 1 \end{bmatrix}; \tag{7}$$

For thermoelastic materials which undergo a martensitic transformation, the presence of multiple phases arises from a nonconvex free energy $\tilde{\psi}(\boldsymbol{E}, \theta)$. The free energy function has multiple minima corresponding to the various phases and variants: a single minimum corresponding to austenite phase above transformation temperature θ_T and minima corresponding to two martensite variants below transformation temperatures.

This is expressed as $\hat{\psi}(\boldsymbol{E}, \theta) > \hat{\psi}(\boldsymbol{0}, \theta)$ for $\theta > \theta_T, \forall \boldsymbol{E} / = \boldsymbol{0}$ and $\hat{\psi}(\boldsymbol{E}, \theta) > \hat{\psi}(\boldsymbol{E}_i, \theta)$ for $\theta < \theta_T, \forall \boldsymbol{E} \neq \boldsymbol{E}_i, i = 1, 2$. The variants of martensite have equal energy at all temperatures $\hat{\psi}(\boldsymbol{E}_1, \theta) = \hat{\psi}(\boldsymbol{E}_2, \theta)$.

As described by Vedantam and Abeyaratne [35], the Helmholtz free energy ψ can be expressed as a polynomial expansion of the strain invariants of the parent phase in order to incorporate the symmetries of the phases. The explicit form of the free energy in two dimensions is given by

$$\psi = \tilde{\psi}(I_1, I_2, \theta), \tag{8}$$

where $I_1 = E_{11} + E_{22}$ and $I_2 = E_{11}E_{22}$ are the strain invariants.

A simple Landau polynomial expansion of the free energy with temperature-dependent coefficients is considered

$$\begin{aligned} \tilde{\psi}(I_1, I_2, \theta) = d_0(\theta) + d_1(\theta)I_1^2 + d_2(\theta)I_1^4 \\ + d_3(\theta)I_2 + d_4(\theta)I_2^2 + d_5(\theta)I_2^4. \end{aligned} \tag{9}$$

and the coefficients are obtained following the algorithm given in [35].

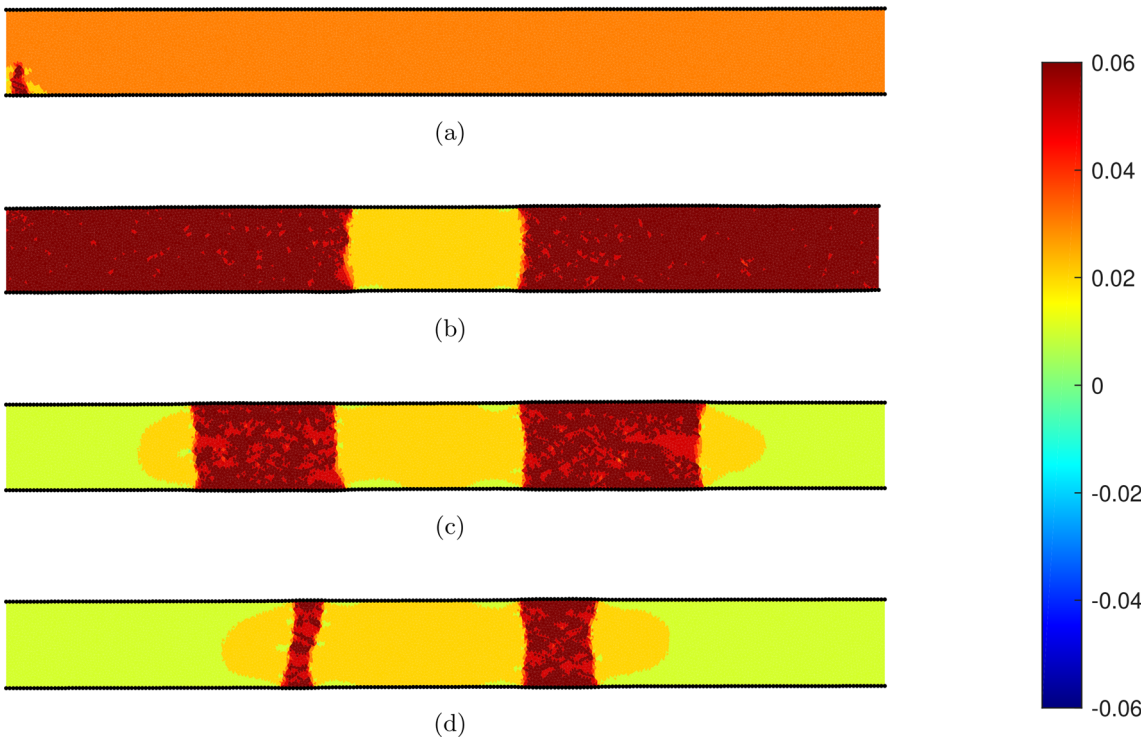

Fig. 2 Uniaxial tension of an SMA wire: **a** initial nucleation occurs at $\varepsilon = 0.028$, **b** the transformation fronts propagate inward upon further loading at strain $\varepsilon = 0.05$, **c** unloading occurs through four interfaces, **d** snapshot of the microstructure during an unloading strain of $\varepsilon = 0.017$. The domain is colored according to the value of the strain component E_{11} as indicated in the color bar on the right-hand side (Color figure online)

$$d_1 = 11.92, \quad d_2 = 1558.33 - 19.50(\theta - \theta_R),$$
$$d_3 = 15.50 - 0.40(\theta - \theta_R),$$
$$d_4 = -8116.67 - 41(\theta - \theta_R),$$
$$d_5 = 2.67 \times 10^8,$$

where $\theta_R = 300\,\mathrm{K}$ is a reference temperature. The transformation temperature is $\theta_T = 310\,\mathrm{K}$ for the parameters chosen. The transformation temperature is the average of martensite start and austenite finish temperatures following the Ginzburg–Landau formalism [35]. The transformation temperature is a typical value chosen from among the range of compositions available reported for CuAlNi alloy [36].

2.3 Computational Aspects

We consider SMA wires of dimensions ϕ 0.5 mm × 5 mm. This domain is discretized into about 7.5×10^3 particles. Thus each Delaunay triangle is of side of about 80 μm. Assuming that the simulations represent plane stress conditions and that the specimen depth is 1 mm and the density[1] is 7150 kg/m^3, the mass of the particle is about 2×10^{-8} kg. We load the specimen at constant displacement rate in all the simulations by fixing the particles on the left boundary and displacing the particles on the right boundary by small increments for each time step. The forces on the particles on the right surface are calculated at each time step. The total force on all the particles on the right surface divided by the area is the taken to be the stress. The stress is plotted against the nominal strain obtained by the displacement of the right surface divided by the initial length of the wire. The strain rate is taken to be $\dot{\varepsilon} = 5 \times 10^{-4}$/s and the total loading strain is $\varepsilon_T = 0.05$. The total number of loading time steps is 10^6. Thus we take the time step of the simulations to be 10^{-4} s. Equations (1) are solved using the velocity-Verlet algorithm as described in [30]. The temperature is taken as a control parameter and specified uniformly throughout the domain. In this work, all the high-temperature simulations of pseudoelastic behavior are performed by setting $\theta = 340\,\mathrm{K}$ and the low-temperature simulations are performed by setting $\theta = 225\,\mathrm{K}$ in the free energy given by Eq. (9).

[1] The free energy used in this study is based on the energy developed for CuAlNi alloy by Vedantam and Abeyaratne [35]. Thus, we use the density of CuAlNi SMA here.

3 Results and Discussion

3.1 Phase Transformations in SMA Wire

We first simulate the behavior of an SMA wire to examine the formation and evolution of the microstructure. The wire is loaded at a temperature of 340 K. The transformation to a single variant martensite and the corresponding evolution of this microstructure are shown in Fig. 2 at various time steps. As the wire is loaded, the strain-induced martensite nucleates at the two ends of the wire due to the stress concentration due to loading and grows inward during the loading. Upon unloading, the parent austenite phase is recovered completely.

Similarly, the microstructure at 225 K is shown in Fig. 3. The two variants of martensite are represented by the red- and blue-colored triangles for strain component $E_{11} = +0.05$ and $E_{11} = -0.05$, respectively. Upon loading, the initially twinned microstructure is detwinned with increasing strain and the entire domain is transformed into a single variant. The twin boundaries are oriented at $\pm 45^{\circ}$ with the austenite lattice satisfying the compatibility conditions arising from the twinning equation [31].

3.2 SMA Composite: Single Wire

We next consider the mechanical behavior of a composite material with a single SMA wire centrally placed inside the matrix. We consider three composite materials with different Young's moduli of the matrix. The three composites

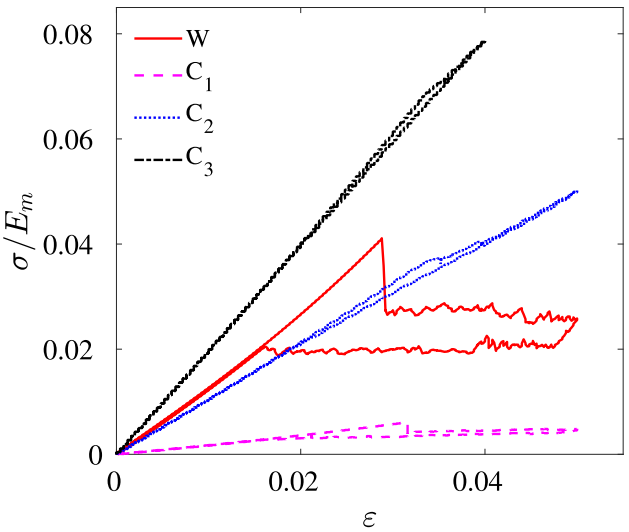

Fig. 4 Effective stress–strain curves for the wire and the three composites

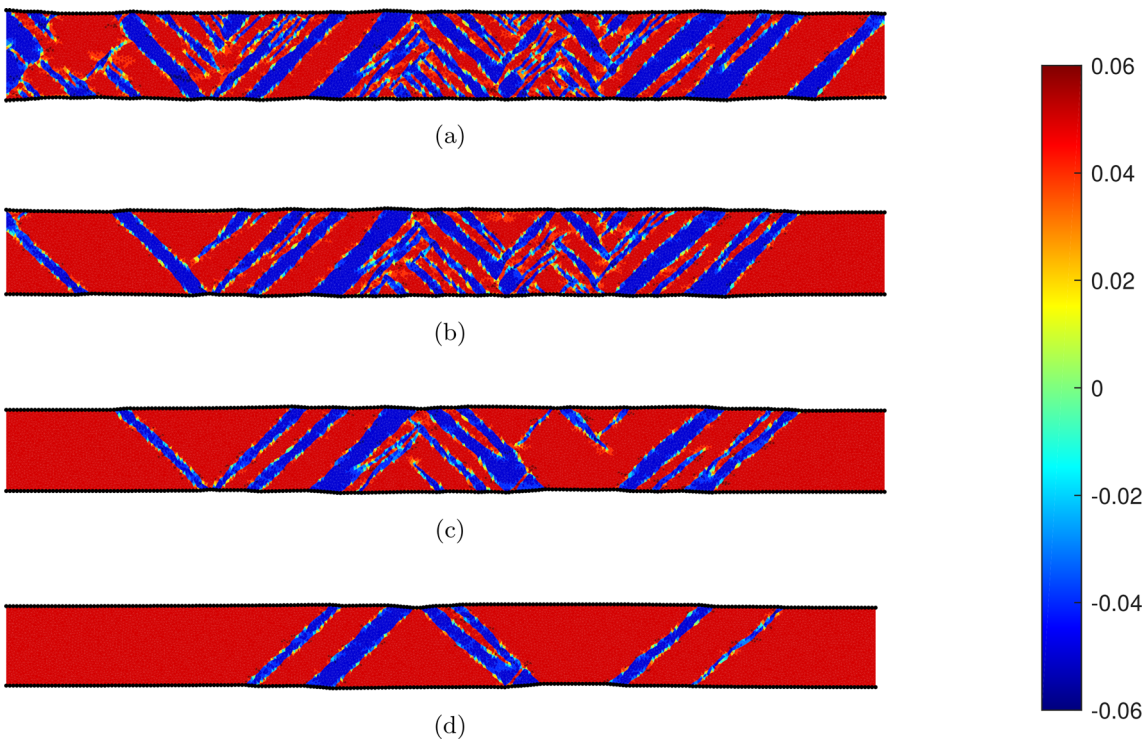

Fig. 3 Detwinning of an SMA wire at $\theta = 225$ K: **a** initial twinned microstructure at $\varepsilon = 0.006$. Snapshot of detwinned microstructure at **b** $\varepsilon = 0.017$, **c** $\varepsilon = 0.028$ and **d** $\varepsilon = 0.039$. The domain is colored according to the value of the strain component E_{11} as indicated in the color bar on the right-hand side (Color figure online)

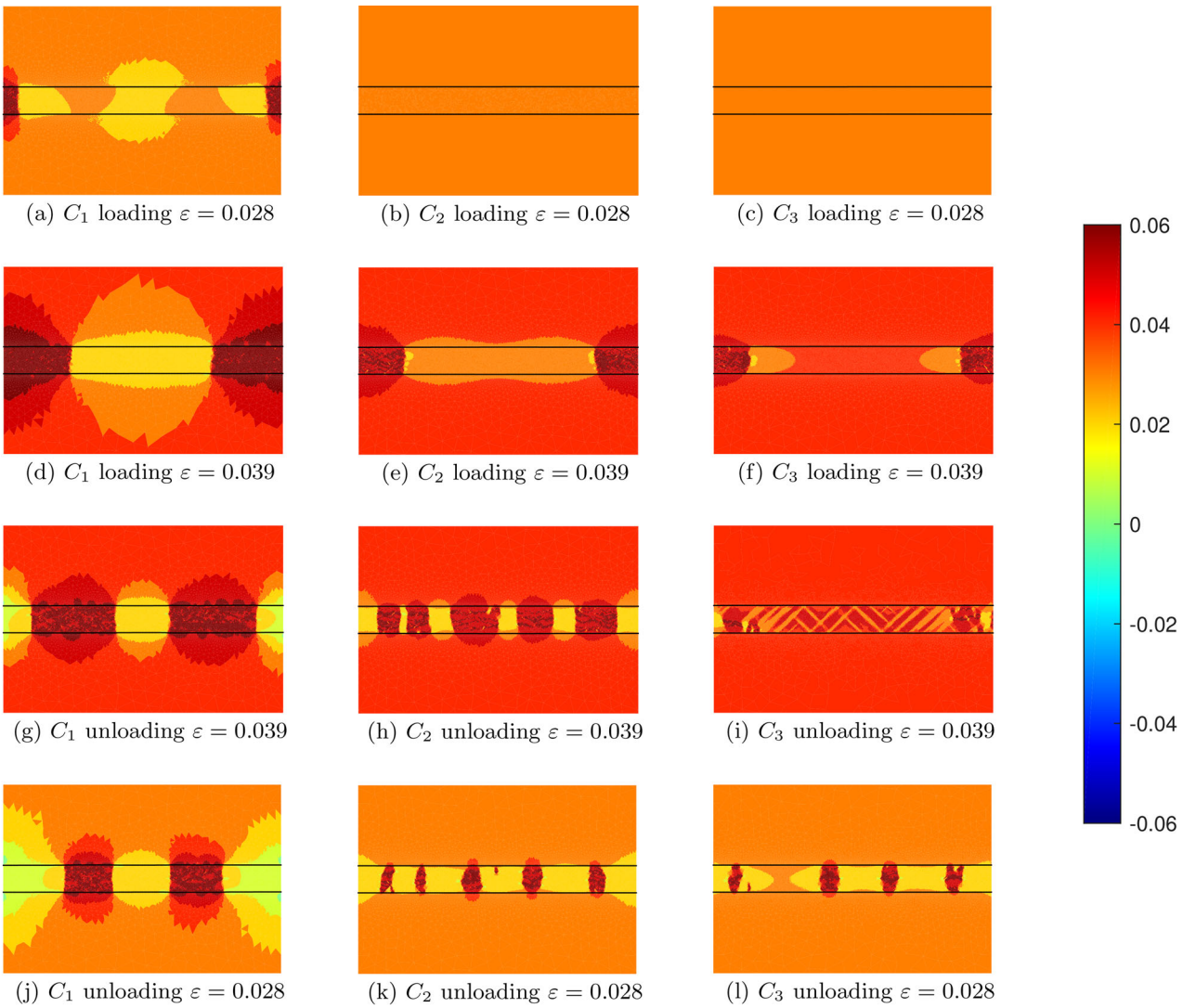

Fig. 5 Microstructural evolution in the three composites at two intermediate stages of loading and unloading. The wire is initially in the austenitic phase. The domain is colored according to the value of the strain component E_{11} as indicated in the color bar on the right-hand side (Color figure online)

are named C_1, C_2 and C_3 and Young's modulus of the matrix is taken to be $E_{C1} = E/20$, $E_{C2} = E$ and $E_{C3} = 2E$, respectively, where E is the Young's modulus of the austenite phase of the SMA wire. We consider the interfacial strength of the wire and matrix to be very high and hence debonding is not considered.

3.2.1 Pseudoelasticity

We first consider the mechanical response of the composite at a temperature greater than the transformation temperature θ_T. The wire is in an austenitic phase in the unstressed state. The stress–strain curves for the SMA wire and the three composites are compared in Fig. 4.

The evolution of the microstructure in the composites is shown in Fig. 5. The left column comprising of Fig. 5a, d, g, j shows the evolution of the microstructure in the composite C_1, whereas the middle and right columns show evolution of the microstructure in the composites C_2 and C_3, respectively. The top two rows show the microstructure at two intermediate loading time steps, whereas the bottom two rows show the microstructure at two intermediate unloading time steps. Each of the rows represents the same time step (equivalently the same strain) of loading and unloading for all the composites.

It can be seen from Fig. 5a–c that the nucleation has occurred earlier in C_1, which has the lowest matrix Young's modulus. The presence of the stiffer matrix in the

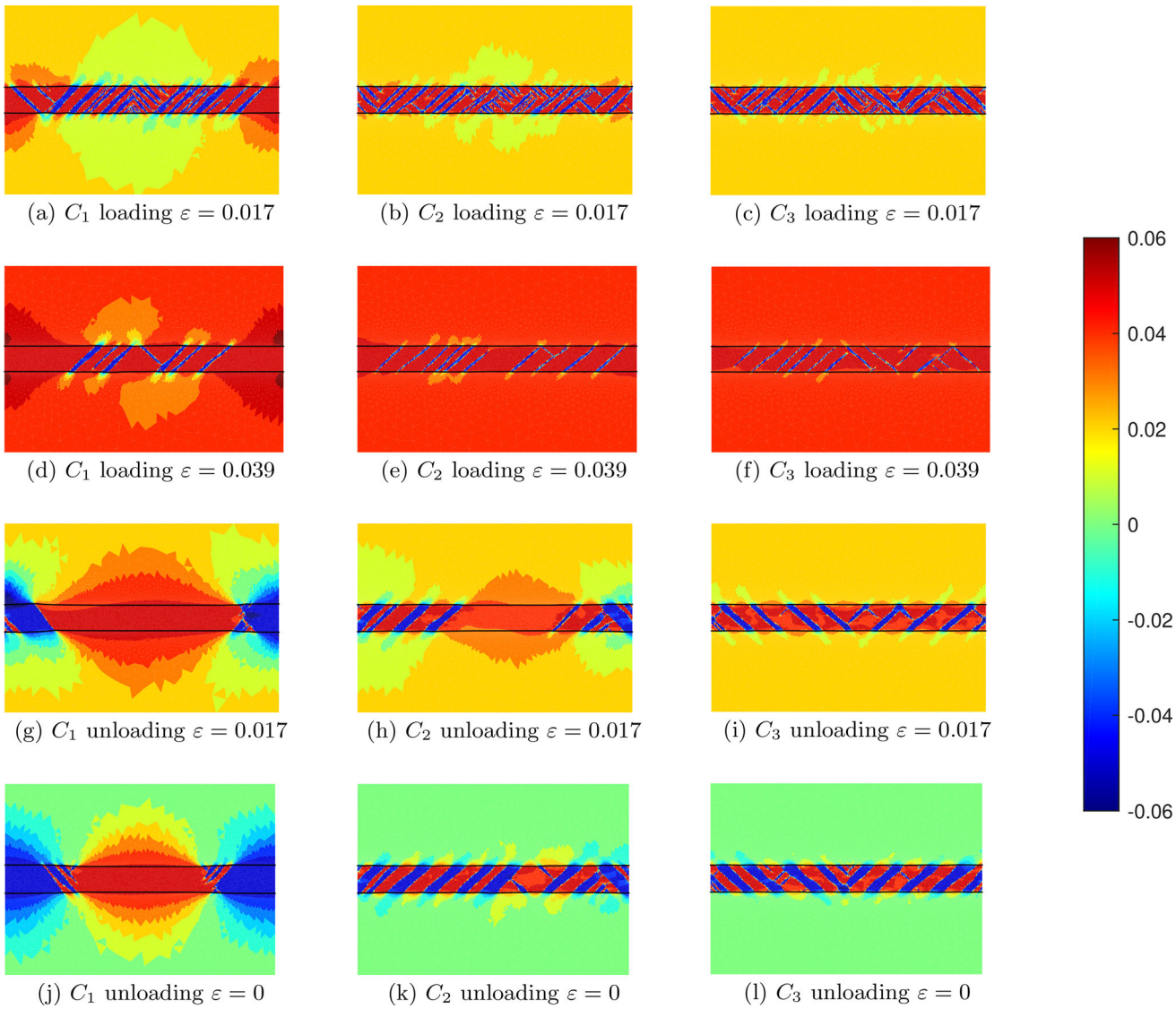

Fig. 6 Evolution of the microstructure in the three composites at two intermediate stages of loading and unloading. Initially the wire is in a twinned martensite phase. The domain is colored according to the value of the strain component E_{11} as indicated in the color bar on the right-hand side (Color figure online)

composites C_2 and C_3 suppresses gradients in the strain along the wire at the initial loading. However, at a higher strain value of $\varepsilon = 0.039$, nucleation is seen in the composites C_2 and C_3 as well. The nucleation occurs near the ends of the wire (near the loading boundary) and propagates inward. The strain gradient occurred due to martensitic transformation in the wire is carried over to the composite with softer matrix (C_1). However, the composite with stiffer matrix (C_3) takes almost no strain from the wire.

During unloading, nucleation of austenite occurs at the ends and in the center of the wire in composite C_1 similar to the unloading microstructure observed in the wire (Fig. 2c). In the composites C_2 and C_3, it is very interesting to note that, during unloading, the nucleation of the austenite occurs in a much more finely distributed manner. Particularly, in Fig. 5i, the inhomogeneity in the strain across the wire causes the formation of fine inclined bands. The role of the matrix in suppressing the gradients in the strain up to a later stage of unloading causes this significant difference in the resultant microstructure.

3.2.2 *Detwinning*

We now examine the case in which the wire is placed in the matrix and cooled to below the transformation temperature.

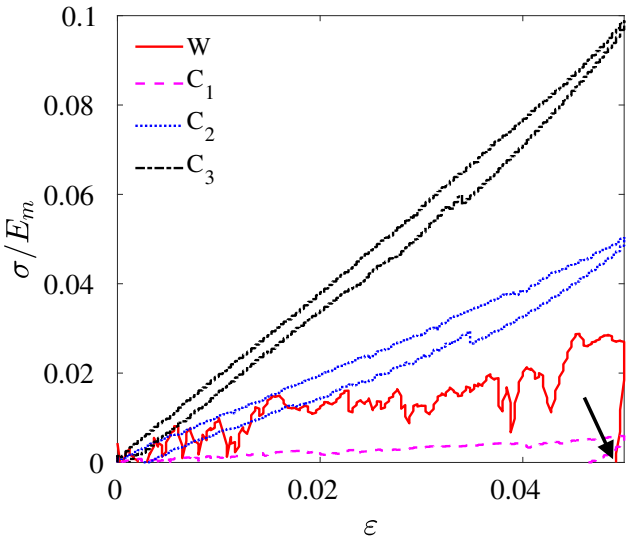

Fig. 7 Effective stress–strain curves of the SMA wire and the three types of composites. The temperature is taken to be lower than the transformation temperature and the wire is initially in a twinned martensite phase. The retained strain upon unloading the wire is indicated by an arrow in the figure

The microstructure at various stages of loading is shown in Fig. 6. As in the previous subsection, the columns show the microstructure for each composite and the rows show the microstructure at a particular strain with the top two rows showing intermediate loading states and the bottom two rows showing intermediate unloading states.

The microstructure at early stages of loading shows fine twinned variants of martensite in all the three composites (Fig. 6a–c). The variants are oriented at $\pm 45^\circ$ to the horizontal as expected. A strain in the matrix can be observed due to the twinning of the wire. Upon further loading, detwinning occurs mostly from the boundaries. It is also interesting to observe that the -45° variants are more susceptible to detwinning under this uniaxial loading. In comparison, in the detwinning of the wire without the confinement induced by the matrix, the bands oriented at both $\pm 45^\circ$ seem to be approximately equally susceptible to detwinning as seen in Fig. 3.

The corresponding stress–strain curves are shown in Fig. 7. During unloading, we note from the stress–strain curves that for the wire and C_1 composite (with a low Young's modulus matrix), the detwinning strain is retained upon unloading as expected. It is well known that the recovery of the detwinning strain occurs only through a heating step in which the material is heated above the transformation temperature.

However, when the matrix is stiffer (as in composites C_2 and C_3), the detwinning process is itself reversible. Upon unloading (as seen in Fig. 6h, i, k l), the martensite twins reappear. We also show the microstructure in composite C_1 under compression in Fig. 6g, j for the purpose of comparison. It is noted that this microstucture is obtained by applying a compressive force to the composite. In the composites C_2 and C_3, the twinned microstructure reappears upon unloading with a tensile force. The martensite variants appear throughout the domain and gradually thicken upon further unloading.

3.3 SMA Composite: Wire Interaction Effects

We now examine the interaction between two wires. In this work, we consider a particular geometry in which the distance of the centers of the wires is 1.1 mm. The effect of the volume fraction arising due to different separation distances will be considered in the future work. The pseudoelastic effect during mechanical loading above the transformation temperature as well as the detwinning of the twinned wire below the transformation temperature are studied in the following sub-sections.

3.3.1 Pseudoelasticity

Figure 8 shows the microstructure at different stages of loading and unloading. As before, the columns show the microstructure in composites C_1, C_2 and C_3 and the rows represent the various stages of loading and unloading. The composite C_1 has a significant strain gradient in the matrix and this results in early nucleation compared to C_2 and C_3. The effect of the matrix in enhancing the interactions between the wires appears in the form of increasing the fineness of the resulting microstructure during loading as well as unloading.

The effective stress–strain curves for the loading and unloading of the two wire composites are shown in Fig. 9a. It is clearly observed that the width of the hysteresis loops is greater than that of the single wire case. This may be due to the interaction effects between the two wires. In order to examine this possibility, we also compare with simulations on a composite with a single wire of diameter 1 mm. The stress–strain curves are presented in Fig. 9b. It is seen that the width of the hysteresis loops for the composites C_2 and C_3 is approximately twice that of the single wire of diameter 0.5 mm. From this, it appears that the larger hysteresis width in a composite with two wires is due to the interactions between the wires. This indicates that composites with closely spaced wires may be more effective in vibration damping applications.

3.3.2 Detwinning

Figure 10 shows the microstructure at different stages of loading and unloading for the composite with two wires at a temperature below the transformation temperature. The

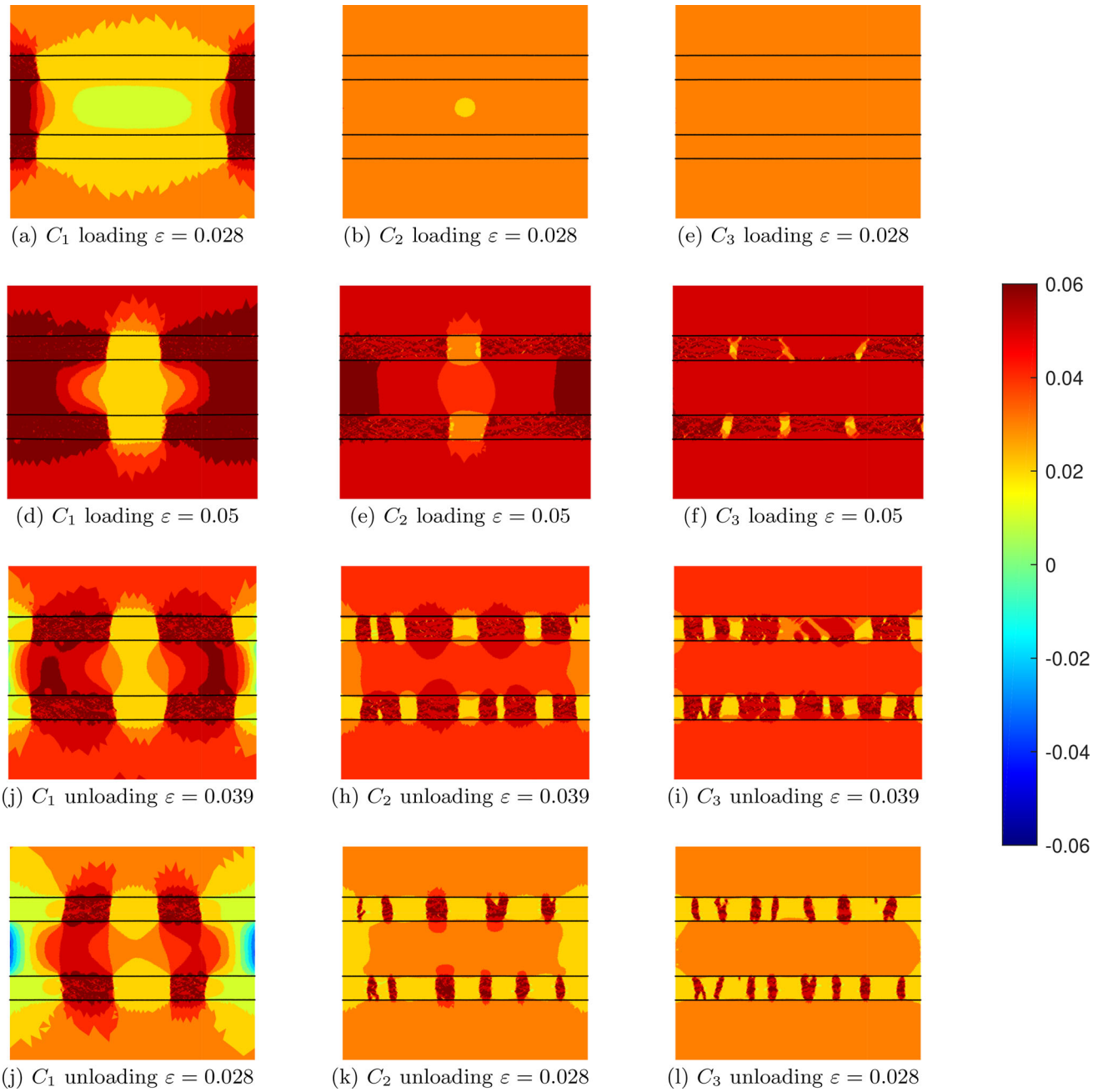

Fig. 8 Evolution of the microstructure in the three composites at two intermediate stages of loading and unloading. The effect of the interaction between the SMA wires appears in the form of a strain gradient in the matrix. The wires are initially in the austenitic phase. The domain is colored according to the value of the strain component E_{11} as indicated in the color bar on the right-hand side (Color figure online)

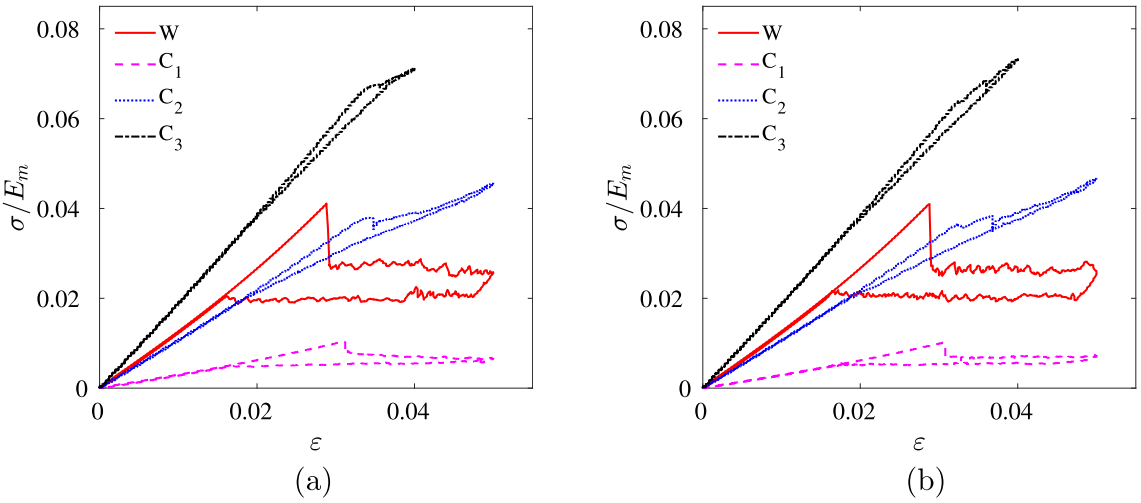

Fig. 9 Effective stress–strain curves of uniaxial loading of the wire compared to the three types of composites considered. **a** The composites are reinforced with two wires of diameter 0.5 mm. **b** The composites are reinforced with one wire of diameter 1 mm

wires are initially in the martensite phase. We note that the microstructure is not symmetric in the two wires and this is due to the presence of the matrix, which causes an interaction between the wires. At higher strain values, only very thin laths of martensite are present. Both $\pm 45^\circ$ orientations of the martensite laths are present.

Upon unloading, the C_1 composite remains in the detwinned state and Fig. 10g, j and m shows the martensite formation upon compressive loading. However, in the other two composites, a reappearance of the twinned martensite is observed due to the matrix stress. Upon unloading to $\varepsilon = 0.017$ as shown in Fig. 10k, the second variant appears from the ends of the wires and further unloading results in the second variant forming thicker laths as shown in Fig. 10n. The composite with a stiffer matrix (C_3) shows a more complete retwinning process compared to C_2.

The effective stress–strain curves for the two-wire composite are shown in Fig. 11. As discussed in Sect. 3.3.1, the widths of the hysteresis loops are more than twice those for the single-wire composites due to the wire interaction effects.

4 Conclusions

In this work, we use a recently developed discrete particle approach to study SMA composites. The model incorporates the continuum free energy into three-body interactions between particles allowing for a very general constitutive description. Using this approach, a detailed description of the formation and evolution of microstructure in the SMA composite is presented under uniaxial loading. Three cases of SMA composites are considered with matrix having Young's modulus less than, equal to and greater than that of the SMA wire.

The following conclusions are obtained from this study:

1. The rich microstructure arising from both mechanical and thermal loading is described to fine detail by the discrete particle model.
2. The effect of the matrix Young's modulus is quite significant on the resulting microstructure of the wire. A matrix with a higher Young's modulus delays the phase transformation in the wire.
3. In composites with a matrix with higher Young's modulus, detwinning of the martensite variants appears reversible and twins reform upon unloading.
4. The interaction between two wires causes significant differences in the stress–strain curves. Particularly, the

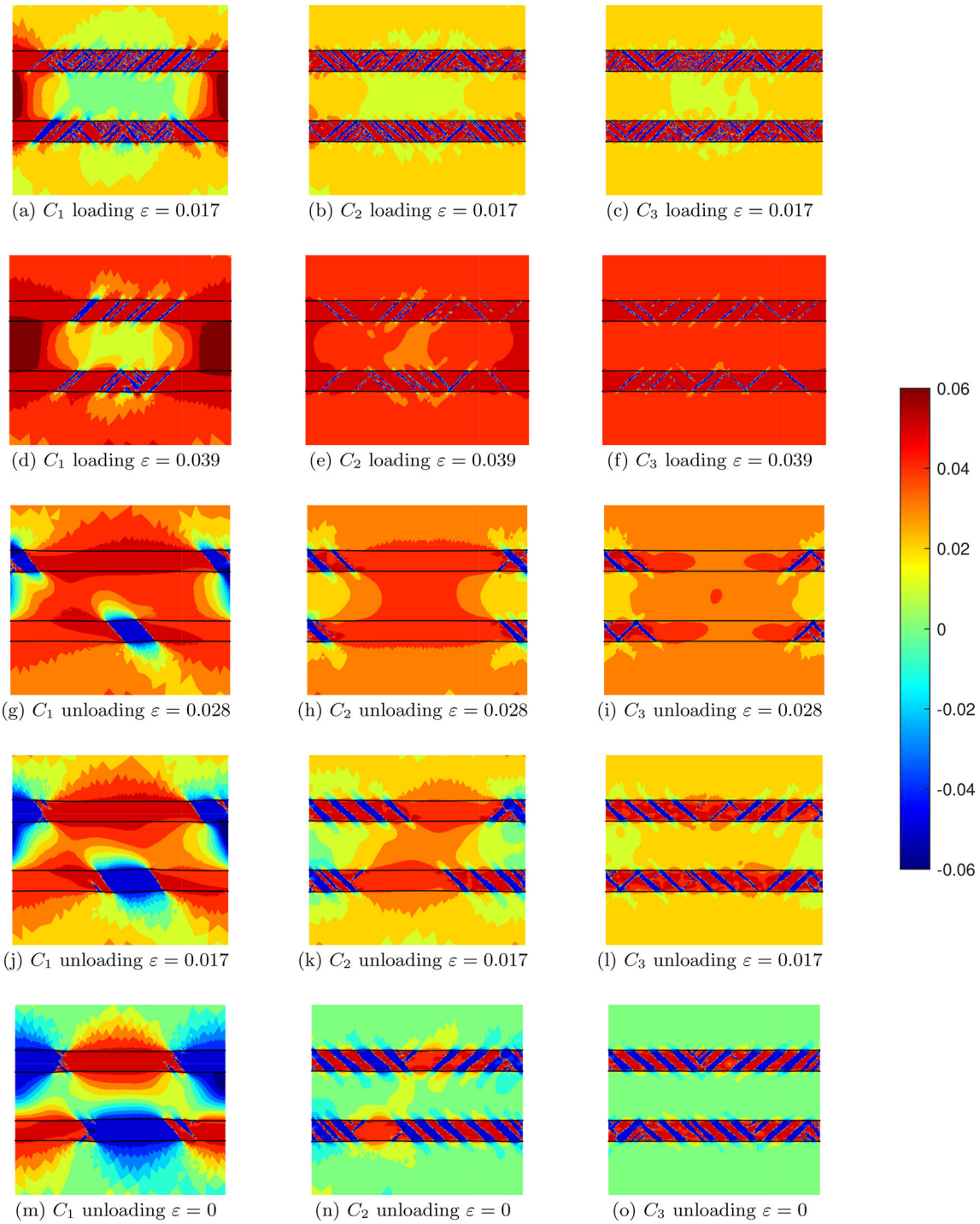

Fig. 10 Evolution of the microstructure in the three composites (reinforced with two SMA wires) at two intermediate stages of loading and three stages of unloading. Initially the wire is in a twinned martensitic phase. The domain is colored according to the value of the strain component E_{11} as indicated in the color bar on the right-hand side (Color figure online)

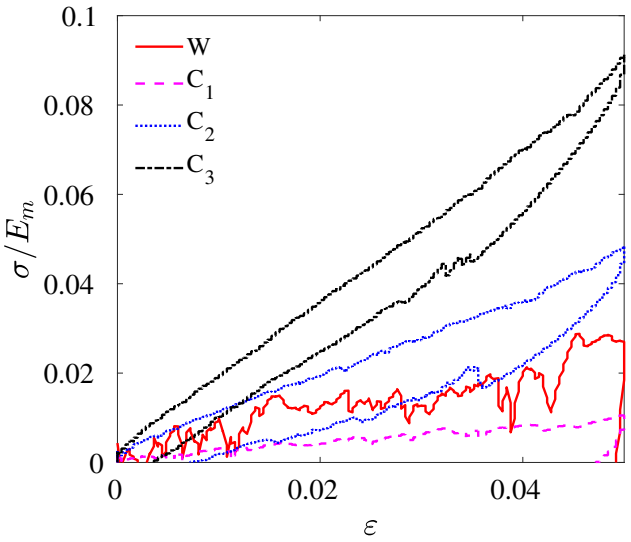

Fig. 11 Effective stress–strain curves of uniaxial loading of the wire compared to the three types of composites considered. The composites are reinforced with two wires. The temperature is taken to be lower than the transformation temperature

width of the hysteresis loops in composite with two wires is greater than that seen in composites with one wire with twice the diameter.

These conclusions are expected to be important for designing composites with optimal vibration dampening and self-healing properties. Further studies on the role of debonding of the wires are important to model the mechanical response of SMA composites.

Acknowledgements We acknowledge the use of the computing resources at HPCE, IIT Madras. The authors wish to acknowledge and thank Dr. Mahendaran Uchimali for his participation in numerous critical discussions and his suggestions.

References

[1] Mangalgiri P D, *Bull Mater Sci* **22** (1999) 657.
[2] Puglia D, Biagiotti J, and Kenny J M, *J Nat Fibers* **1** (2005) 23.
[3] Yun W, Chengyan D, Bin Y, Lu Z, and Shenshen C, *Compos Struct* **202** (2018) 818.
[4] Karunagaran N, Bharathiraja G, Muniappan A , and Yoganandam K, *Mater Today Proc* **22** (2020) 1078.
[5] Mohammadkhani P, Jalali S S, and Safarabadi M, *Compos Struct* **256** (2021) 112992.
[6] Cohades A, and Michaud V, *Adv Ind Eng Polym Res* **1** (2018) 66.
[7] Karger K J, and Keki S, *Polymers* **10** (2017) 34.
[8] Lester B, Baxevanis T, Chemisky Y, and Lagoudas DC, *Acta Mech* **226** (2015) 3907.
[9] Kumar P K, and Lagoudas D C, *Introduction to Shape Memory Alloy* (2008).
[10] Mohd J J, Leary M, Subic A, and Gibson M A, *Mater Des* **56** (2014) 1078.
[11] Antonucci V, and Martone A, *Phenomenology of Shape Memory Alloys* (2021) p 115.
[12] Aboudi J, Arnold S, and Bednarcyk B, *Micromechanical Analysis of Smart Composite Materials* (2013) p 677.
[13] Raghavan J, Bartkiewicz T, Boyko S, Kupriyanov M, Rajapakse N, and Yu B, *Compos B Eng* **41** (2010) 214
[14] Sun M, Wang Z, Yang B, and Sun X, *Compos Struct* **171** (2017) 170.
[15] Rodrigue H, Wang W, Bhandari B, Han M W, and Ahn S H, *Compos B Eng* **82** (2015) 152.
[16] Humbeeck J V, *J Alloys Compd* **355** (2003) 58.
[17] Jonnalagadda K, Kline G E, and Sottos N R. *Exp Mech* **37** (1997) 78.
[18] Payandeh Y, Meraghni F, Patoor E, and Eberhardt A, *Mater Des* **39** (2012) 104.
[19] Zhang X, Feng P, He Y, Yu T, and Sun Q, *Int J Mech Sci* **52** (2010) 1660.
[20] Scalet G, and Auricchio F, *Shape Memory Alloy Engineering (Second Edition)* (2021) p 345.
[21] Sacco E, and Artioli E, *Shape Memory Alloy Engineering (Second Edition)* (2021) p 291.
[22] Marfia S, and Vigliotti A, *Shape Memory Alloy Engineering (Second Edition)* (2021) p 247.
[23] Puglisi G, and Truskinovsky L, *J Mech Phys Solids* **48** (2000) 1.
[24] Puglisi G, and Truskinovsky L, *J Mech Phys Solids* **50** (2002) 165.
[25] Zhong Y, and Zhu T, *Acta Mech* **75** (2014) 337.
[26] Pun G P P, and Mishin Y, *J Phys Condens Matter* **22** (2010) 395403.
[27] Chen H, Xu Y, Jiao Y, and Liu Y, *J Mater Sci Eng A* **659** (2016) 234.
[28] Salviato M, Zappalorto M, and Quaresimin M, *Compos Part A Appl Sci Manuf* **48** (2013) 144.
[29] Msekh M A, Silani M, Jamshidian M, Areias P, Zhuang X, Zi G, He P, and Rabczuk T, *Compos B Eng* **93** (2016) 97.
[30] Uchimali M, Rao B C, and Vedantam S, *Comput Methods Appl Mech Eng* **366** (2020) 113052.
[31] Uchimali M, Rao B C, and Vedantam S, *Acta Mater* **205** (2021) 116528.
[32] Wang G, Ostaz A A, Cheng A H D, and Mantena P R, *Comput Mater Sci* **44** (2009) 1126.
[33] Nikolic M, Karavelic E, Ibrahimbegovic A, and Miščevic P, *Arch Comput Methods Eng* **25** (2018) 753.
[34] Uchimali M, *Mech Adv Mater Struct.* https://doi.org/10.1080/15376494.2021.1909787
[35] Vedantam S, and Abeyaratne R, *Int J Non Linear Mech* **40** (2005) 177.
[36] Palánki Z, Daróczi L, Lexcellent C, and Beke D L, *Acta Mater* **55** (2007) 1823.